4

Diffusion-Weighted Chemical Shift Imaging of Human Brain Metabolites at 7T

This chapter was adapted from:

A. E. Ercan, A. Techawiboonwong, M.J. Versluis, A.G. Webb and I. Ronen, "Diffusion-weighted chemical shift imaging of human brain metabolites at 7T", *Magnetic Resonance in Medicine*, Volume 73, Issue 6, pages 2053-2061, 2015.

Abstract

Diffusion-weighted chemical shift imaging (DW-CSI) of brain metabolites poses significant challenges associated with the acquisition of spectroscopic data in the presence of strong diffusion weighting gradients. A reproducible DW-CSI acquisition and processing scheme is presented, one that addresses most of the potential sources of instability and which provides reproducible and anatomically-meaningful diffusion-weighted and apparent diffusion coefficient (ADC) metabolite maps. A real-time navigator-based acquisition scheme is used, allowing instantaneous re-acquisition of corrupted k-space data and post-processing correction of gradient-induced phase fluctuations. Eddy current correction based on the residual water resonance is implemented and significantly improves the data quality. Highly reproducible diffusion-weighted metabolite maps of three highest concentration brain metabolites are shown. The navigator-based accept/reject strategy and the post-acquisition corrections significantly improved the stability of the DW-CSI signal and the reproducibility of the resulting DW-CSI maps. Metabolite ADC values obtained in this work could be related to the underlying tissue cellular composition. In conclusion, robust investigation of DW-CSI of brain metabolites is feasible and can potentially provide complementary information to that obtained from more sensitive but less specific methods such as diffusion tensor imaging.

4.1 Introduction

DIFFUSION-WEIGHTED MRI (DWI) and diffusion tensor imaging (DTI) are the most commonly used neuroimaging tools for obtaining information on microscopic structural features of tissue and their modulation by disease processes [1, 2]. The link between diffusion tensor metrics, e.g. fractional anisotropy (FA) and apparent diffusion coefficient (ADC), and tissue microstructural features such as the degree of myelination and cellular/axonal density and size is, however, difficult to establish. DWI lacks compartmental specificity since its signal source, namely water, originates from multiple tissue compartments, and its interpretation is further complicated by rapid exchange of water molecules through cell membranes during the diffusion times used in these experiments [3]. Diffusion-weighted MR spectroscopy (DW-MRS) explores the diffusion properties of intracellular metabolites, such as N-acetylaspartate, creatine and phosphocreatine, and total choline compounds, in the millimolar concentration range. The relatively low concentration of these metabolites dictates a significantly lower sensitivity than that of DWI-based methods, but their cellular and compartmental specificity allows for compartment-specific assessment of tissue microstructure and thus has the potential of providing unique information on cell-specific structure and physiology, and sensitively reporting on specific deficits linked with disease. Single volume (SV) DW-MRS has been shown to yield meaningful and reproducible results in the rodent [4–8], monkey [9, 10], and human brain [11–17], and has been applied to study pathological changes in neural tissue microstructure in various diseases in the human brain, e.g. acute cerebral ischemia [18, 19], brain tumors [19, 20], multiple sclerosis [21], mitochondrial myopathy, encephalopathy, lactic acidosis, and stroke-like episodes (MELAS) syndrome [22] and psychiatric disorders [23].

The single-voxel nature of DW-MRS limits its application to specific white matter tracts or arbitrarily selected regions of interest. An early work showed the possibility of obtaining DW-CSI maps of acetone and water in phantom [24]. Since then, only a few attempts have been made so far at obtaining maps of the diffusion properties of brain metabolites with DW chemical shift imaging (DW-CSI) [25–27]. The long scanning times these experiments require limit their clinical applicability, and so far they have been characterized by a lack of robustness and reproducibility. The instability of DW-CSI can be attributed to several factors including the multi-shot nature of the acquisition, combined with the low signal to noise ratio (SNR) of the metabolite resonances, and the relatively high gradient strength needed for adequate diffusion weighting of the slow diffusing metabolites. These factors result in strong inter-shot phase and amplitude fluctuations as well as strong eddy currents, which degrade the resulting DW spectra.

In this study, we show for the first time a DW-CSI method that yields robust, reproducible and anatomically-meaningful diffusion-weighted maps of the main brain metabolites: N-acetylaspartate + N-acetylaspartylglutamate (NAA + NAAG = tNAA), creatine + phosphocreatine (Cr + PCr = tCr) and total soluble choline compounds (tCho). The method efficiently suppresses the amplitude fluctuations during data acquisition and corrects gradient-induced phase fluctuations as well as the strong eddy currents generated by the diffusion-weighting gradients.

4.2 Materials and methods

4.2.1 Human subjects

A total of five healthy volunteers (two female, three male, age: 34.4 ± 10.1 years) participated in this study. Two of the volunteers were scanned twice for the reproducibility investigation, and one was scanned for demonstration of the navigator-based corrections. The study adhered to the Leiden University Medical Center Institutional Review Board guidelines and informed consent was obtained from all subjects prior to the study.

4.2.2 Data acquisition

4.2.2.1 MRI scanner/Hardware

All experiments were performed on a 7 Tesla Achieva Philips whole-body MRI scanner (Philips Healthcare, Best, The Netherlands) equipped with gradient coils capable of a maximum gradient strength of 40 mT/m and a slew rate of 200 T/m/s. A head coil consisting of a quadrature birdcage transmit and 32-channel phased array receive (Nova Medical Inc., Wilmington, MA, USA) was used for all measurements.

4.2.2.2 Anatomical images

A short survey scan and a sensitivity encoding (SENSE) reference scan were followed by a 3D T_1-weighted gradient echo acquisition for accurate planning of the diffusion-weighted experiment and for the assessment of the gray (GM) and white matter (WM) tissue fractions within each CSI voxel via post-processing. Imaging parameters were: field of view (anterior-posterior(AP), foot-head(FH), right-left(RL)): 246×246×174 mm^3, resolution 0.85×0.85×1.00 mm^3, TR/TE=4.94/2.17 ms. Total scan time was 3 minutes.

4.2.2.3 CSI Pulse Sequence

The two-dimensional diffusion weighted chemical shift imaging (DW-CSI) pulse sequence is shown in Figure 4.1. The PRESS (Point Resolved Spectroscopy, [28]) sequence was chosen as the base spectroscopic sequence. Diffusion weighting used bipolar gradients for minimization of eddy currents [29]. Based on our experience in developing the single volume DW-MRS sequences, the implementation of bipolar gradients has several beneficial aspects in addition to the minimization of eddy currents; the use of available time for gradients is maximized, so higher b-values can be reached for the same gradient strength and TE, and the cross-terms with background gradients is efficiently compensated. The phase-encoding gradient, originally located immediately after the excitation pulse in the sequence supplied by the vendor, was repositioned after the trailing edge of the second lobe of the refocusing diffusion gradient, allowing 25-30 data points to be acquired immediately following the second lobe of the refocusing diffusion weighting gradient and before the echo maximum. These data points were used as a phase and amplitude navigator, described later. A supra-callosal axial slice was selected for the DW-CSI experiment (see Figure 4.2 for the planning of the CSI experiment). Field of view: 96×96 mm^2, matrix size: 12×12 with standard elliptical k-space filtering, zero-filled to a 16×16 matrix. The PRESS sequence was applied in volume-selective mode, where the dimensions of the volume of interest (VOI) were 48×42×8 mm^3 (AP, RL, FH). This resulted in a voxel size of 6×6×8 mm^3 in the reconstructed CSI data set, and a matrix of 8×7 = 54 encoded voxels within the selected VOI.

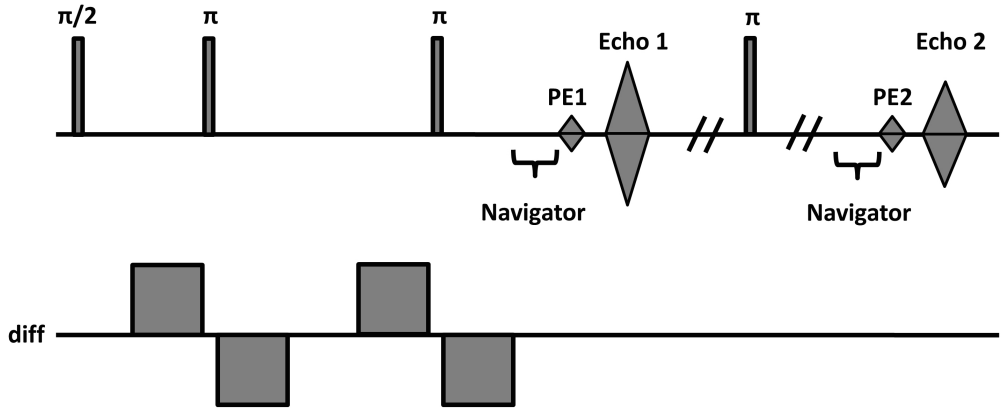

FIGURE 4.1: Schematic representation of the PRESS-based 2D DW-CSI pulse sequence, where bipolar gradients are used for diffusion weighting. The phase encoding (PE) gradient is placed after the second lobe of the refocusing diffusion gradient and before the echo maximum such that 25-30 navigator data points are acquired prior to the phase-encoding step.

Data were collected with cardiac gating using a peripheral pulse unit (PPU). The delay between the trigger and the excitation pulse at the beginning of the sequence was set to 230 ms in order to minimize fluctuations induced by cardiac pulsation. The resulting duration of the water suppression scheme was 223 ms. TR was set to three cardiac cycles (about 3 seconds), and the center RF frequency was set to that of tNAA (2.0 ppm). A turbo spectroscopic imaging (TSI) mode with two echo acquisitions (TE = 100/205 ms) was used, and 256 sample points were acquired for each of the two echoes with a spectral bandwidth of 5000 Hz. Water suppression with variable pulse power and optimized relaxation delays (VAPOR) [30] was used. The efficacy of the water suppression was de-optimized during the diffusion-weighted acquisitions by increasing the delay between the last pulse of the VAPOR block and the excitation pulse to 250 ms. This was done so that sufficient residual water signal was present for the navigator and for eddy current correction. For each DW-CSI scan, 5 consecutive CSI data sets were acquired: one without water suppression with b = 0 s/mm^2, to allow for accurate local frequency corrections; one data set with water suppression and no diffusion weighting (b = 0 s/mm^2) and three diffusion-weighted data sets where the diffusion weighting was applied in three orthogonal directions aimed to maximize available gradient strength: $[-0.5, 1, 1]$, $[1, -0.5, 1]$ and $[1, 1, -0.5]$[31]. The gradient duration was set to 20 ms, the time between the two bipolar gradients was 14 ms and the diffusion time (time between the first lobe of the dephasing group and the second lobe of the rephasing group) was 50 ms. The gradient amplitude was 35 mT/m, resulting in a b-value of 2870 s/mm^2. The total scan time for each subject was about 15-20 minutes.

One phantom experiment was performed at room temperature on the GE-MRS "Braino" phantom, which contained the following metabolites: NAA (12.5 mM); creatine (10 mM); choline (3 mM); Ins (7.5 mM); Glu (12.5 mM) and lactate (5 mM). One diffusion weighting direction was used, TR was set to 2 seconds, and the b-value was lowered to

936 s/mm^2. An additional SV-DWS experiment was performed, with the same conditions and experimental parameters and the VOI for this experiment was 2×2×2 cm^3.

Navigator-based data reacquisition scheme: For each diffusion-weighted condition, 5 consecutive measurements with no phase encoding were made prior to acquisition of the phase-encoded data. The sum of the moduli of 6 navigator data points (points 5 - 10) was calculated for each of these measurements, and the highest sum was selected as the *amplitude reference*. An empirically-determined threshold of 85% of the amplitude reference was defined as the amplitude threshold for the following acquisitions. This threshold was then used in real-time as an accept/reject criterion for subsequent acquisitions for that diffusion condition such that for each k-space location, data that fell below the threshold were re-acquired. An upper limit for the number of reacquisitions was set to 100 for each diffusion condition.

4.2.3 Post-Processing and Data Analysis

4.2.3.1 CSI data post-processing

All data analyses were performed off-line. Raw data (k-space/time domain data sets from each individual receive coil) were exported from the scanner and an in-house MATLAB® (Mathworks, Natick, MA, USA) routine was used to perform the following operations: (a) individually phase and combine the data from each of the 32 receiver coils, weighted according to the SNR of each channel; (b) use the phase information from the navigator to correct for phase fluctuations introduced by the diffusion gradients (see later for details); (c) perform Hanning filtering on the k-space data, spatial and temporal Fourier transforms, voxel-wise frequency shift corrections using the non-water suppressed data; (d) perform voxel-wise eddy current correction using the residual water peak present in the free induction decay (FID), isolated by performing a linear prediction singular value decomposition (LPSVD) procedure on the FID and using the spectral components in a 1ppm region around the water resonance [32]; (e) remove the residual water resonance using the water spectral information obtained with the LPSVD routine in the eddy current correction stage; (f) export the 5 data matrices (data without water suppression, water-suppressed data with b = 0 s/mm^2 and the 3 diffusion-weighted data sets) in Philips format (SDAT/SPAR) for further spectral analysis.

4.2.3.2 Removal of diffusion-induced phase fluctuations using the phase navigator

The navigator time-domain data were zero-filled to 128 points and line-broadened. Following a Fourier transformation, a coarse spectrum of the navigator was obtained. The phase for each acquisition was then estimated from the residual water, and diffusion induced phase fluctuations were removed using the formula:

$$S_{ij,m}(corr) = S_{ij,m} \cdot \frac{\exp\left(i\theta_{\mathrm{nav}}(ij, b=0)\right)}{\exp\left(i\theta_{\mathrm{nav}}(ij, m)\right)} \tag{4.1}$$

where $S_{ij,m}$ is the FID obtained at the k-space location ij and diffusion condition m, and $\theta_{\mathrm{nav}}(ij, m)$ is the navigator phase at this condition. It should be noted that at the condition $b = 0$ the phase includes the effect of the shift of the CSI matrix in image space.

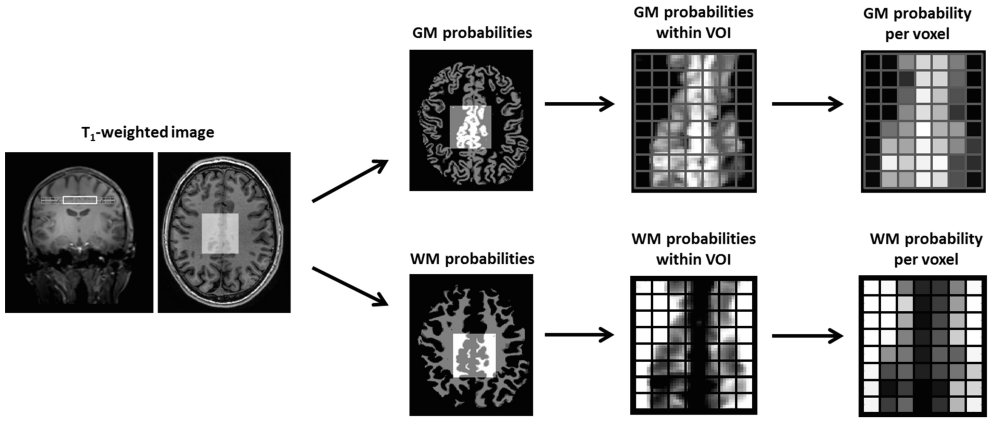

FIGURE 4.2: The procedure of voxel-wise estimation of gray and white matter probabilities within the VOI. The gray and white matter tissue probabilistic maps are obtained following the brain extraction from the T_1-weighted image. The DW-CSI VOI is then overlaid on the corresponding location in the tissue maps such that the gray and white matter tissue probabilities within the VOI can be assessed. The gray and white matter tissue probabilities were then down-sampled to the resolution of the voxels of the DW-CSI within the VOI.

4.2.3.3 Tissue segmentation and estimation of gray and white matter fractions in CSI voxels

Voxel-wise estimation of white matter, grey matter and cerebrospinal fluid (CSF) fractions was performed with in-house MATLAB® routine, using tissue probability maps generated from the high resolution T_1-weighted image. Brain-confined tissue probability maps were generated by first applying the FSL tools Brain Extraction Tool (BET) [33] and FMRIB's Automated Segmentation Tool (FAST) [34] to the T_1-weighted volume. The MATLAB routine then matched the voxels in the tissue probability maps with the corresponding CSI voxels, and the final step was to average the tissue probabilities within each CSI voxel to yield an average voxel-wise gray matter and white matter fraction. Tissue fractions were defined according to: $f_{GM} = \frac{p_{GM}}{p_{GM}+p_{WM}}$ and $f_{WM} = \frac{p_{WM}}{p_{GM}+p_{WM}}$, where f_{GM} and f_{WM} are the GM and WM fractions, p_{GM} and p_{WM} are the gray matter and white matter probabilities. p_{CSF}, the CSF probability, was excluded since the concentration of metabolites in the CSF is negligible. The process is illustrated in Figure 4.2.

4.2.3.4 Spectral quantification and ADC calculation

Quantification of the CSI spectra for each condition was done using LCModel [35]. The LCModel output table for each condition, containing the peak estimation and Cramér-Rao lower bounds (CRLB) for each metabolite for each voxel location, was read into MATLAB for calculation of the ADC for each metabolite of interest according to:

$$ADC_{i,j} = -\frac{1}{3b}\sum_{n=1}^{3}\ln\left(\frac{S_{i,j,n}(b)}{S_{i,j}(0)}\right) \tag{4.2}$$

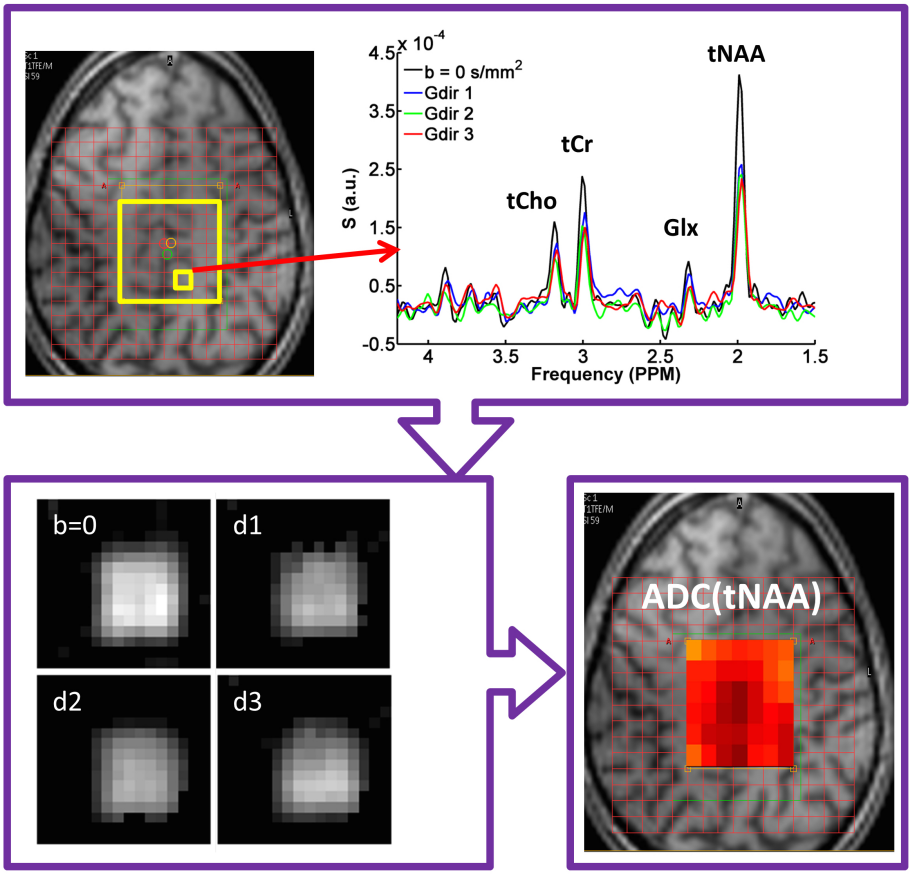

FIGURE 4.3: A schematic description of the acquisition and processing pipeline for DW-CSI.

where $S_{i,j,n}(b)$ is the signal intensity at the CSI location (i, j) obtained with the diffusion-weighting gradient in the direction n, $S(0)$ is the signal intensity without diffusion-weighting, and b is the b-value used in the experiment. Voxels with CRLB values higher than 10% for any of the four diffusion-weighting conditions were discarded.

Figure 4.3 describes the overall process from planning and acquisition to the generation of metabolite ADC maps, in this case for tNAA.

4.3 Results

4.3.1 Artifact removal from DW-CSI data using navigator information

The effects of the navigator-based artifact correction schemes used in our experiments on the DW-CSI data are shown in Figure 4.4, panels a-d, where representative tNAA DW-CSI maps for b = 0 s/mm^2 and one diffusion weighted condition acquired with b = 2870 s/mm^2 are shown. Panel (a) shows the CSI map of tNAA acquired at b = 0 s/mm^2. It is seen that the tNAA signal is well localized within the selected VOI represented by a

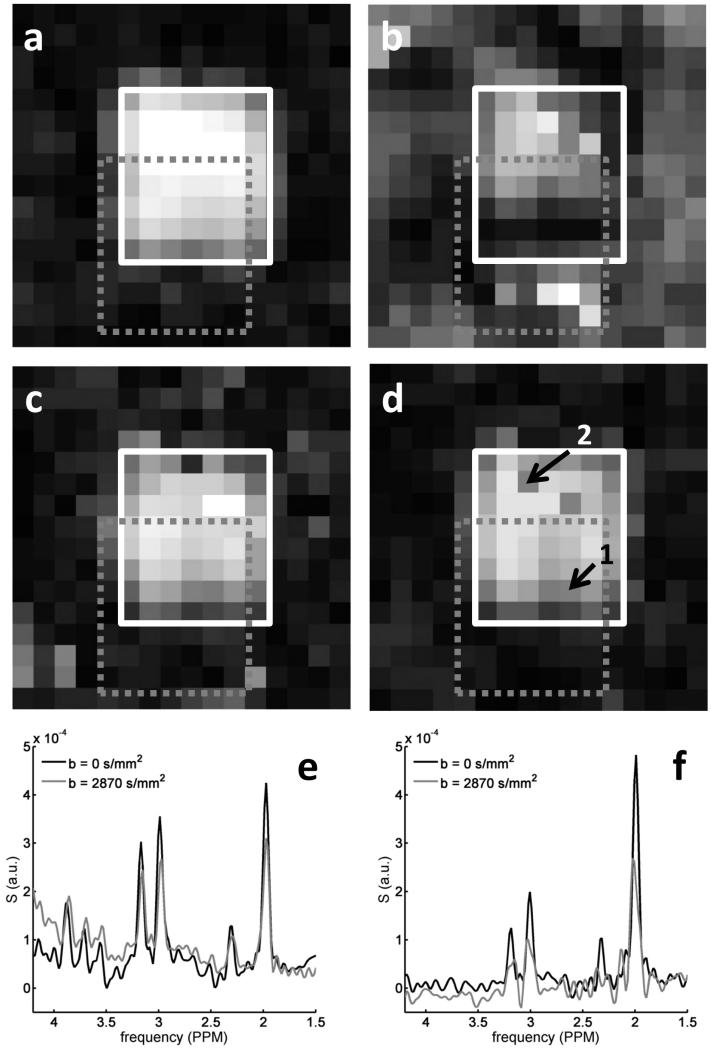

FIGURE 4.4: (a-d) DW-CSI maps of tNAA obtained at b = 0 s/mm^2 (a) and b = 2870 s/mm^2 from one diffusion-weighting condition processed in three different ways: (b) no navigator-based re-acquisitions and no removal of phase fluctuations are performed (c) removal of phase fluctuations is performed, without using the navigator-based re-acquired data (d) navigator-based reacquisitions are used, and removal of phase fluctuations is performed. Solid white rectangle: selected VOI at the tNAA singlet resonance frequency (2.0 ppm). Dashed gray rectangle: shifted VOI at the water resonance frequency (4.65 ppm). (e-f) The spectra acquired at b = 0 s/mm^2 (black line) and with diffusion weighting at b = 2870 s/mm^2 applied in one direction (gray line). Voxel 1 lies within the intersection of metabolite and water VOIs where sufficient water signal is obtained, thus an efficient eddy correction could be performed. Voxel 2 is located outside the water VOI, and the water-based eddy current correction was not effective. Line-broadening of 5 Hz and zero-filling to 1024 points were applied to all spectra.

solid rectangle. The dashed rectangle represents the shifted VOI that comprises the water signal. Panels b-d show DW-CSI tNAA maps obtained for the first diffusion weighting direction, $[1,1,-0.5]$, at b = 2870 s/mm^2 and processed in three different ways: Panel (b) shows the map obtained without using navigator-based re-acquisitions and without removal of the phase fluctuations induced by the diffusion weighting gradients. It can be seen that the localization of the signal to the preselected VOI is severely compromised and significant portion of the signal within the VOI is lost as well. In panel (c) removal of the phase fluctuations was performed, but the navigator based re-acquired data were not used. Localization of the tNAA signal within the selected VOI is improved, but there are still visible artifactual signal contributions from outside the selected VOI. Panel (d) shows the tNAA DW-CSI map obtained following both phase fluctuation removal and use of reacquired data. The number of reacquired excitations was 15 and the total number of k-space encoded excitations was 56. The tNAA data is now firmly localized within the preselected VOI. It should be noted that this data set was acquired without cardiac triggering so the degrading effects of both phase and amplitude fluctuations could be made clearly visible. In our standard protocol, the addition of cardiac triggering further reduces the typical number of reacquired excitations, and helps improve the overall quality of the DW-CSI data.

The effect of the eddy current correction based on the water signal is shown in Figure 4.4, panels (e-f). Panel (e) shows the spectra obtained from voxel *1* in Figure 4.4 panel (d), which lies within the intersection region between the VOI selected at the tNAA frequency (2.0 ppm) and the one selected at the water frequency (4.65 ppm). Spectra are shown for data acquired at b = 0 s/mm^2 (black) and b = 2870 s/mm^2 (gray). There is no discernible difference in the metabolite line shape and the quality of the spectrum is sufficiently restored by the eddy current correction procedure. The presence of the residual water peak shoulder can be seen in both spectra. Panel (f) shows spectra obtained from voxel *2* in Figure 4.4 panel (d), which lies inside the tNAA VOI, outside the water VOI and on the margin of the tCr/tCho VOI. The diffusion weighted spectrum is severely distorted by eddy currents, and as expected, the tCr, tCho peaks and other peaks at lower resonance frequencies are attenuated. For further analyses, voxels were chosen from the region where the water-based eddy current correction was effective.

4.3.2 DW-CSI Spectra and Metabolite ADC maps

Figure 4.5 shows typical spectra obtained from a CSI voxel within the preselected VOI where sufficient water signal was obtained. The four spectra shown in each panel were obtained with b = 0 s/mm^2 and b = 2870 s/mm^2 applied in the three diffusion gradient directions specified in the methods section. Typical CRLB values for tNAA, tCr and tCho were 3%, 4% and 5% at b = 0 s/mm^2 and 5%, 6% and 7% at b = 2870 s/mm^2, respectively. Typical ADC maps for tNAA, tCr and tCho are shown in Figure 4.6. The maps show the voxels within the preselected VOI for which the CRLB values for all four conditions were lower than 10%. Overlaid in solid line is the shifted VOI for the water peak. The intersection of the two regions contains the voxels in which the eddy current correction based on the water peak was reliable, and the ADC values from these voxels are used in the reproducibility and the tissue-based ADC analyses shown later. ADC values for the three metabolites calculated from the single volume and CSI phantom experiments ensured the accuracy of the CSI results; For the SV DW-MRS experiments the ADC values were 0.55×10^{-3} mm^2/s, 0.76×10^{-3} mm^2/s and 0.84×10^{-3} mm^2/s for tNAA, tCr and tCho,

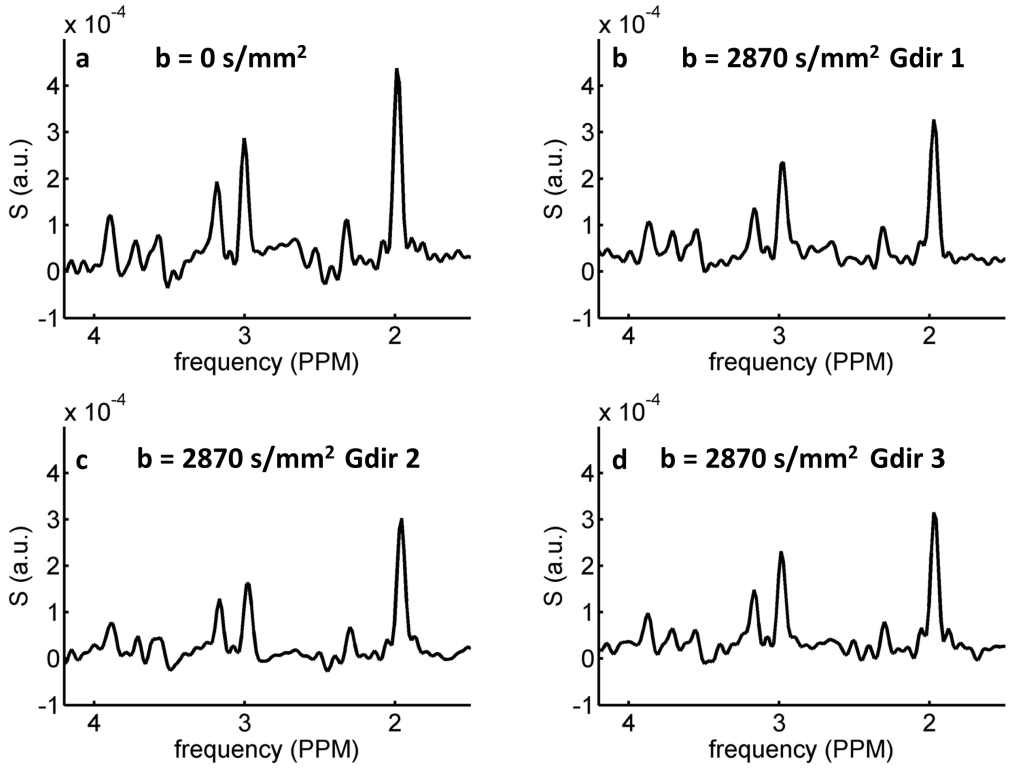

FIGURE 4.5: Typical spectra obtained from a single CSI voxel within the VOI at b = 0 s/mm^2 (a) and b = 2870 s/mm^2 applied in 3 diffusion gradient directions (b-d). Line-broadening of 5 Hz and zero-filling to 1024 points were applied to all spectra.

respectively, and for the CSI experiments the ADC values over the preselected VOI were 0.57×10^{-3} ± 0.02 mm^2/s, 0.73×10^{-3} ± 0.03 mm^2/s and 0.87×10^{-3} ± 0.03 mm^2/s for tNAA, tCr and tCho, respectively.

4.3.3 Reproducibility of DW-CSI data in repeated acquisitions

Pearson's linear coefficient (r) was calculated as a measure of correlation between the tNAA values obtained from the two scans from one subject, and the resulting values were r = 0.99, 0.96, 0.97 and 0.95 for b = 0 s/mm^2 and the three diffusion-weighted acquisitions (b=2870 s/mm^2), respectively for this subject. The correlation between the ADC values calculated from these two data sets resulted in r = 0.76. For the second subject who had the two consecutive DW-CSI acquisitions, r values corresponding to the correlation between the tNAA values obtained from the two scans were r = 0.96, 0.97, 0.94 and 0.97 for b = 0 s/mm^2 and the three diffusion-weighted acquisitions, respectively. The correlation between the ADC values calculated from these two data sets resulted in r = 0.68.

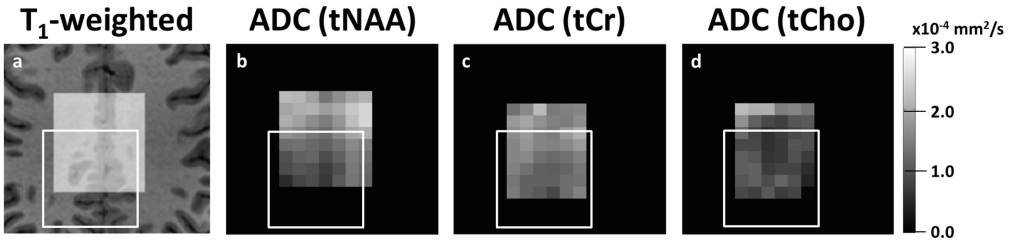

FIGURE 4.6: Metabolite ADC maps for tNAA (b), tCr (c) and tCho (d) and the corresponding T_1-weighted image (a) from one of the subjects. The shifted VOI at the water frequency is shown in white. Only voxels from the regions intersecting with the water VOI were selected for further analyses.

4.3.4 Tissue-based analysis of metabolite ADC

Metabolite ADC values from the DW-CSI data sets were co-analyzed with information on gray/white matter tissue fractions from the corresponding voxels to yield tissue specific information on metabolite ADC values. In Figure 4.7, ADC values for tNAA, tCr and tCho are shown as a function of the GM fraction in the corresponding voxels for one of the subjects. For this data set, Pearson's r values for the correlation between ADC(tNAA), ADC(tCr) and ADC(tCho) and white matter fraction were 0.69, 0.60 and 0.04, respectively.

Extrapolation of the linear fit, such as the one shown in Figure 4.7, to gray matter fractions of 0 and 1 allowed the estimation of metabolite ADC in white matter and gray matter, respectively. Table 4.1 shows metabolite ADC values for GM and WM estimated for each subject and for the entire cohort, as well as the correlation coefficients between the metabolite ADC and the GM fraction. ADC(tNAA) values were significantly negatively correlated with gray matter fraction, and less so were the ADC(tCr) values. The ADC(tCho) showed no significant correlation with gray matter fraction.

The group-averaged metabolite ADC values for GM and WM are shown in Figure 4.8. ADC(tNAA) was significantly higher in white matter than in gray matter (p-value < 0.001, paired 2-tail t-test). ADC(tCr) was also significantly higher in white matter than in gray matter (p-value < 0.005). No significant difference was found between ADC(tCho) in GM and WM.

4.4 Discussion

In this study we have introduced a robust and reproducible DW-CSI acquisition and processing scheme that yields spatially resolved diffusion weighted maps of tNAA, tCr and tCho in the human brain. The results are in agreement with previous tissue-based explorations of metabolite ADC using SV DW-MRS, and are anatomically meaningful, as will be later discussed. To our knowledge, this is the first study to fully demonstrate the feasibility of DW-CSI in humans in which instabilities in signal acquisition associated with the multi-shot nature of DW-CSI acquisition have been successfully resolved. Additionally, the combination with tissue probability maps obtained from high resolution T_1-weighted images allowed estimation of metabolite ADC values in gray and white matter.

Both phase and amplitude signal fluctuations during acquisition required the introduc-

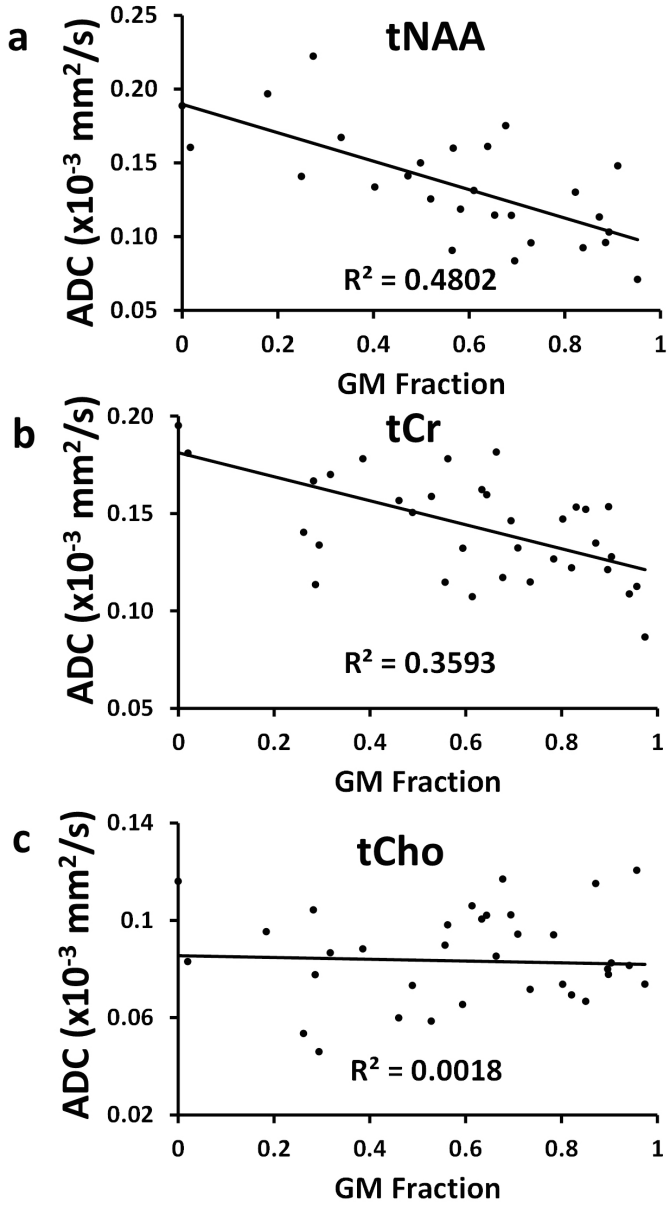

FIGURE 4.7: Correlation between voxel-wise gray matter tissue fraction with the corresponding tNAA (a), tCr (b) and tCho (c) ADC values, taken from one subject. The linear fit (black line) and resulting R^2 are displayed for each metabolite.

TABLE 4.1: Metabolite ADC values estimated for pure gray matter and pure white matter tissues for each subject and for the cohort. Pearson's r value represents the linear correlation of the ADC values as a function of gray matter fraction in the DW-CSI voxels and is presented with the corresponding p-value. NS, not significant.

ADC ($\times 10^{-3}$ mm^2/s)			
		tNAA	
Subject	GM	WM	$r(P)$
S1 # 1	0.10	0.14	-0.47 (0.004)
S1 # 2	0.13	0.16	-0.66 (<0.001)
S2	0.11	0.16	-0.48 (0.004)
S3	0.11	0.17	-0.56 (<0.001)
S4 # 1	0.12	0.17	-0.32 (<0.001)
S4 # 2	0.09	0.19	-0.48 (<0.001)
Group	0.11 ± 0.01	0.17 ± 0.02	-0.57 ± 0.10
		tCr	
Subject	GM	WM	$r(P)$
S1 # 1	0.10	0.14	-0.54 (<0.001)
S1 # 2	0.14	0.19	-0.59 (<0.001)
S2	0.13	0.14	-0.10 (NS)
S3	0.17	0.18	-0.14 (NS)
S4 # 1	0.15	0.17	-0.24 (NS)
S4 # 2	0.12	0.18	-0.60 (<0.001)
Group	0.13 ± 0.02	0.17 ± 0.02	-0.37 ± 0.23
		tCho	
Subject	GM	WM	$r(P)$
S1 # 1	0.08	0.10	-0.22 (NS)
S1 # 2	0.12	0.14	-0.30 (NS)
S2	0.12	0.13	-0.01 (NS)
S3	0.11	0.12	-0.11 (NS)
S4 # 1	0.10	0.18	-0.43 (0.02)
S4 # 2	0.08	0.09	-0.04 (NS)
Group	0.10 ± 0.02	0.13 ± 0.03	-0.19 ± 0.15

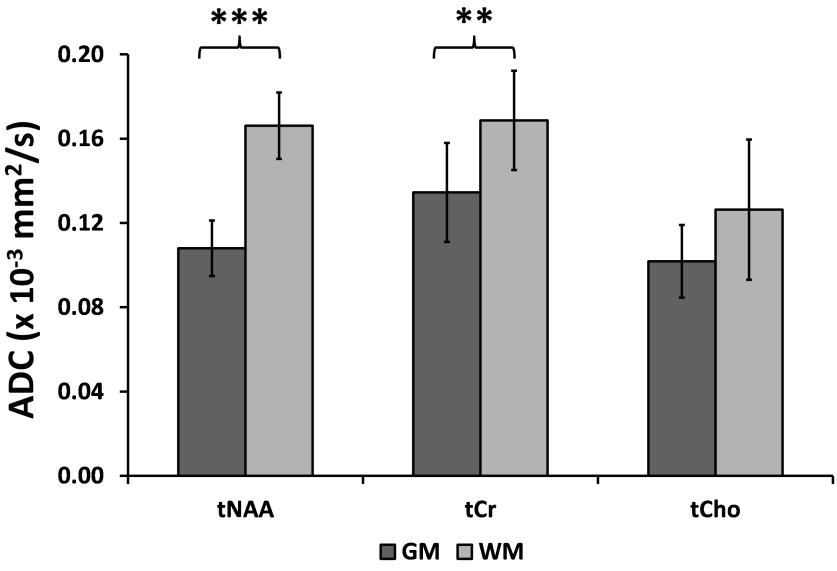

FIGURE 4.8: Group-averaged (n=6) metabolite ADC values in mm^2/s based on the extrapolation of the linear fit to unity tissue fractions for gray matter (dark gray) and white matter (light gray). Significant differences were found between gray and white matter ADC(tNAA) values at p-value < 0.001 (***) and ADC(tCr) at p-value < 0.01 (**). No significant difference was found between gray and white matter ADC(tCho). The error bars indicate the standard deviation.

tion of a navigator, positioned immediately after the diffusion weighting gradients and before the phase encoding step. The need to correct the phase of individual acquisitions in DW-MRS to avoid over-estimation of metabolite ADC has been shown in the case of SV DW-MRS [11, 13, 14]. In SV DW-MRS, phase correction is typically performed on the residual water peak. Applying this approach in DW-CSI required shifting the phase encoding gradient from its original position in the vendor-supplied sequence (immediately following the excitation pulse) to a position immediately before the echo creation, such that there are sufficient data points for which the signal phase and amplitude are dominated by the gradient-induced fluctuations. The dramatic effect of the phase fluctuations induced by the diffusion-weighting gradients is seen in Figure 4.4 panel (b), where the phase correction is not performed.

Our approach for minimizing the amplitude fluctuations in the DW-CSI signal was to introduce a user-controlled real-time reacquisition scheme for individual acquisitions, combined with cardiac triggering. Tight control over the amplitude fluctuations was crucial for the robustness and reproducibility of the resulting data. This is especially true for the acquisition of data near the central k-space region, where most of the signal energy is located and thus where signal drops will have the highest impact on the resulting CSI data quality. The effect of amplitude fluctuations on the data is shown in Figure 4.4 panel (c).

Much of the variation in the diffusion-weighted signal amplitude is caused by cardiac

pulsation [36–38], and in our experience, adding cardiac triggering to the acquisition scheme significantly reduced the number of navigator-based reacquisitions. It is possible to rely solely on the reacquisition scheme for filtering out strong signal fluctuations, but in that case acquisition of the complete data set would become significantly longer. Choosing a higher signal threshold for the re-acquisitions will result in an overall improvement of the resulting DW-CSI data, at the cost of a higher number of re-acquisitions and therefore an increase in scan time. In our work we set the threshold so that signal level below 85% of the reference triggered a re-acquisition. This resulted in reacquisition of about 10% of the total data. The threshold was empirically determined based on a compromise between the increase in total experimental time caused by increased number of re-acquisitions when the threshold was set too high, and the extent of signal fluctuations. The extent of the fluctuations varied across subjects as well as across diffusion weighting directions. This suggests that the orientation of major blood vessels within the VOI as well as the properties of CSF flow may have a strong impact on these fluctuations.

Eddy current correction is crucial in DW-MRS, even when a bipolar diffusion weighting scheme is used. This is shown in Figure 4.4 where voxels with and without efficient eddy current correction are shown. We based our eddy current correction scheme on the residual water signal in each voxel instead of acquiring a full DW-CSI dataset without water suppression and carrier frequency set to the water frequency due to time limitations. To ensure the availability of a sufficiently large water signal in the spectra across the selected VOI, we weakened the water suppression in the diffusion-weighted condition by increasing the delay between the VAPOR scheme and the excitation pulse. This approach is much less affected by inhomogeneity of the B_1 than alternative approaches such as modulating the RF power for the water suppression pulses [16], and thus more suitable for a large preselected VOI. A limitation of the PRESS sequence used in our study is the relatively low bandwidth of the two refocusing pulses, which in turn results in a large chemical shift displacement between the water signal and the other metabolites, shown e.g. in Figure 4.4. Efficient eddy current correction for each metabolite is thus possible in the intersection between the metabolite and the water VOIs, but voxels outside this volume are not properly corrected. Replacing the PRESS sequence with a STEAM partially addresses this issue, since the bandwidth of selective 90° pulses is somewhat higher, albeit with the well-known property of only detecting 50% of the available magnetization. A proper solution will be to incorporate a diffusion weighting scheme with a fully or partially adiabatic spectroscopic sequence, e.g. LASER or semi-LASER [39, 40] where the large bandwidth of the adiabatic pulses will result in a much smaller chemical shift displacement for the water resonance. Another solution is to acquire a full DW-CSI data set without water suppression, with the carrier frequency set to the water frequency. This water data set can be acquired with a shorter TR as well as with a lower spatial resolution, and thus may be incorporated in the protocol if scanning time allows.

The reacquisition and correction strategy implemented here resulted in good reproducibility of the DW-CSI results, as shown in the comparison of two subsequent DW-CSI acquisitions from the same subject. High voxel-by-voxel correlations are reported between acquisitions with the same diffusion weighting conditions, as well as high correlation between the two calculated ADC set of values. Several factors affect the reproducibility of the data, among which are the error in the estimation of the metabolite signal in each voxel (expressed e.g. by the CRLB of the peak estimation), the b-value used for the diffusion weighting, the threshold set on the reacquisition scheme, and patient motion

between the two consecutive scans. The error in signal estimation propagates to the error in estimating the metabolite ADC values (see [2], p.269). The correlation between the two consecutive sets of ADC values was somewhat lower than the correlation between the actual DW-CSI sets possibly due to error propagation properties, as well as due to the smaller relative range of ADC values with respect to their mean, $\Delta ADC/\overline{ADC}$, compared to $\Delta S(CSI)/\overline{S(CSI)}$, the relative range of the DW-CSI signal.

A strong negative correlation of ADC(tNAA)with GM fraction (or alternatively-stated as a strong positive correlation with WM fraction) was found. ADC(tCr) values were negatively correlated with GM fraction as well, albeit to a lesser extent. No correlation was observed between ADC(tCho) and GM fraction. Conversely, the ADC for the three metabolites in white matter, obtained through extrapolation of the ADC data to $f_{GM} = 0$, were higher than their ADC in gray matter, although in tCho this difference did not reach statistical significance. We have reported similar trends in a previous work performed on large single volumes positioned on regions with different content of gray and white matter [16]. A plausible explanation for these findings is the different cellular localization of these metabolites. In white matter, tNAA is almost exclusively axonal, tCr is present in similar concentrations in axons and astrocytes, whereas tCho is predominantly astrocytic [41]. The open-ended axonal geometry and the more "restricted", close-ended astrocytic geometry could thus provide an explanation for the higher ADC(tNAA) and the lower ADC(tCho) in white matter. In gray matter the prevalence of neuronal cell bodies over long range fibers may serve to explain the lower ADC of all three metabolites, and in particular that of tNAA, in gray matter compared to their corresponding ADC values in white matter.

The metabolite ADC values in this study were obtained from a set of relatively small voxels (0.3 cc) and combined with estimated tissue probabilities that provided a wide range of voxel-wise tissue fractions. This allowed us to more accurately estimate tissue-specific metabolite ADC values and in particular metabolite ADC in gray matter, where previous studies, including our own, reported values obtained from large VOIs where partial volume of white matter is unavoidable. In our study, GM metabolite ADC values of all three metabolites were lower than values previously reported [16, 17, 22]. Values previously reported for metabolite ADC in white matter, e.g. for tNAA, are comparable to those reported here [11, 16, 17, 21]. Due to time limitations, the k-space encoding matrix was relatively small (12 × 12). Even though the matrix was significantly larger than the selected VOI and Hanning filtering was used to reduce sinc-like intervoxel bleeding, this choice has significant implications on the point spread function of the voxel-wise spectroscopic data, which then becomes contaminated by signal from adjacent voxels [42]. For simplicity, the average tissue probabilities within a CSI voxel were calculated assuming the voxels to be perfect rectangular cuboids with the same size as the reconstructed voxel size of 6×6×8 mm^3. This limits the tissue specificity of the ADC values calculated here, and emphasizes the need for a more efficient k-space sampling strategy.

The significant increase in sensitivity associated with data acquisition at 7T is offset by several challenges. One is the relative increase in chemical shift displacement of the selected VOI, resulting in inefficient eddy current correction in certain regions. Significant inhomogeneity in the transmit B_1 field at 7T result in large spatial differences in the resulting signal generated by spectroscopic sequences such as PRESS, due to the large flip angles used. This limits the effective field of view to a relatively small region, and for this reason the preselected VOI was set to a relatively small section of the encoded area. Some

of these detrimental effects can be alleviated by using B_1-insensitive adiabatic pulses [39], multiple transmit techniques and padding the head with dielectric material [43]. A bigger VOI selection could also be possible at lower fields such as 3T. One limitation in the way we implemented our DW-CSI acquisition is that CSI data sets under different diffusion weighting conditions are acquired consecutively, or in other words, the inner loop is the k-space position and the outer loop is the diffusion-weighting condition. It is possible to reduce the sensitivity to long-term motional drifts by switching the loop order, and we intend to test this approach in the future. Although the re-acquisition scheme significantly reduced the variance caused by the various instabilities described above, some inconsistencies in our limited data sets, e.g. those in the ADC(tCr) in the repeat scans of subject #4 suggest that there are some sources of variability that our method currently does not account for. For example, we observed that the chosen threshold was not optimal for all three gradient directions in all subjects, and the amplitude fluctuations in a single gradient direction could significantly increase the variability in the resulting metabolite ADC (data not shown). Further investigations are needed to optimize the trigger delay and the corresponding amplitude thresholds, for further improving the robustness of the method. Another limitation of the current implementation is that at this point we have not made use of the parallel imaging capability provided by the multiple receive coil array and the availability of a sensitivity encoding (SENSE) reference scan, resulting in long acquisition times that could limit clinical investigations. Given the relatively high SNR obtained in this study, the acquisition could be shortened by combining the acquisition with SENSE at a reasonable reduction factor [44]. This will also allow the acquisition of full diffusion tensor CSI data sets in a reasonable time, thus opening the way for a methodical comparison between metabolite and water tensor data.

4.5 Conclusions

In summary, we have implemented and showed the feasibility of DW-CSI acquisition and processing scheme in the human brain. The navigator-based corrections implemented in this scheme significantly improve the stability of the DW-CSI signal and the overall quality, reproducibility and robustness of the resulting DW-CSI maps. The method has been shown to work with a two-echo CSI acquisition, allowing for significant shortening of the experimental time. Metabolite ADC values obtained in this work related meaningfully to the underlying tissue cellular composition. Based on previous successful applications of SV DW-MRS to the investigation of neurological disorders, DW-CSI can play a role in increasing the specificity of MR to compartment-specific tissue alterations in disease and lead to identification of new biomarkers for intracellular damage.

4.6 References

[1] D. Le Bihan, J. Mangin, C. Poupon, C. Clark, S. Pappata, N. Molko, and H. Chabriat, "Diffusion tensor imaging: concepts and applications," *Journal of Magnetic Resonance Imaging*, vol. 13, no. 4, pp. 534–546, 2001.

[2] D. Jones, *Diffusion MRI: theory, methods, and applications*. Oxford University Press, 2010.

[3] D. Le Bihan and P. van Zijl, "From the diffusion coefficient to the diffusion tensor," *NMR in Biomedicine*, vol. 15, no. 7-8, pp. 431–434, 2002.

[4] A. van der Toorn, R. Dijkhuizen, C. Tulleken, and K. Nicolay, "Diffusion of metabolites in normal and ischemic rat brain measured by localized 1H MRS," *Magnetic Resonance in Medicine*, vol. 36, no. 6, pp. 914–922, 1996.

[5] M. Wick, Y. Nagatomo, F. Prielmeier, and J. Frahm, "Alteration of intracellular metabolite diffusion in rat brain in vivo during ischemia and reperfusion," *Stroke*, vol. 26, no. 10, pp. 1930–1934, 1995.

[6] J. Pfeuffer, S. Provencher, and R. Gruetter, "Water diffusion in rat brain in vivo as detected at very large b values is multicompartmental," *Magnetic Resonance Materials in Physics, Biology and Medicine*, vol. 8, no. 2, pp. 98–108, 1999.

[7] J. Pfeuffer, I. Tkáč, and R. Gruetter, "Extracellular-intracellular distribution of glucose and lactate in the rat brain assessed noninvasively by diffusion-weighted 1H nuclear magnetic resonance spectroscopy in vivo," *Journal of Cerebral Blood Flow & Metabolism*, vol. 20, no. 4, pp. 736–746, 2000.

[8] W. Dreher, E. Busch, and D. Leibfritz, "Changes in apparent diffusion coefficients of metabolites in rat brain after middle cerebral artery occlusion measured by proton magnetic resonance spectroscopy," *Magnetic Resonance in Medicine*, vol. 45, no. 3, pp. 383–389, 2001.

[9] C. Marchadour, E. Brouillet, P. Hantraye, V. Lebon, and J. Valette, "Anomalous diffusion of brain metabolites evidenced by diffusion-weighted magnetic resonance spectroscopy in vivo," *Journal of Cerebral Blood Flow & Metabolism*, vol. 32, no. 12, pp. 2153–2160, 2012.

[10] J. Valette, M. Chaumeil, M. Guillermier, G. Bloch, P. Hantraye, and V. Lebon, "Diffusion-weighted NMR spectroscopy allows probing of 13 C labeling of glutamate inside distinct metabolic compartments in the brain," *Magnetic Resonance in Medicine*, vol. 60, no. 2, pp. 306–311, 2008.

[11] S. Posse, C. Cuenod, and D. Le Bihan, "Human brain: proton diffusion MR spectroscopy," *Radiology*, vol. 188, no. 3, pp. 719–725, 1993.

[12] C. Kroenke, J. Ackerman, and D. Yablonskiy, "On the nature of the NAA diffusion attenuated MR signal in the central nervous system," *Magnetic Resonance in Medicine*, vol. 52, no. 5, pp. 1052–1059, 2004.

[13] J. Ellegood, C. Hanstock, and C. Beaulieu, "Trace apparent diffusion coefficients of metabolites in human brain using diffusion weighted magnetic resonance spectroscopy," *Magnetic Resonance in Medicine*, vol. 53, no. 5, pp. 1025–1032, 2005.

[14] J. Upadhyay, K. Hallock, K. Erb, D. Kim, and I. Ronen, "Diffusion properties of NAA in human corpus callosum as studied with diffusion tensor spectroscopy," *Magnetic Resonance in Medicine*, vol. 58, no. 5, pp. 1045–1053, 2007.

[15] J. Upadhyay, K. Hallock, M. Ducros, D. Kim, and I. Ronen, "Diffusion tensor spectroscopy and imaging of the arcuate fasciculus," *Neuroimage*, vol. 39, no. 1, pp. 1–9, 2008.

[16] H. Kan, A. Techawiboonwong, M. van Osch, M. Versluis, D. Deelchand, P.-G. Henry, M. Marjańska, M. van Buchem, A. Webb, and I. Ronen, "Differences in apparent diffusion coefficients of brain metabolites between grey and white matter in the human brain measured at 7 T," *Magnetic Resonance in Medicine*, vol. 67, no. 5, pp. 1203–1209, 2012.

[17] J. Ellegood, C. Hanstock, and C. Beaulieu, "Diffusion tensor spectroscopy (DTS) of human brain," *Magnetic Resonance in Medicine*, vol. 55, no. 1, pp. 1–8, 2006.

[18] D. Zheng, Z. Liu, J. Fang, X. Wang, and J. Zhang, "The effect of age and cerebral ischemia on diffusion-weighted proton MR spectroscopy of the human brain," *American Journal of Neuroradiology*, vol. 33, no. 3, pp. 563–568, 2012.

[19] M. Harada, M. Uno, F. Hong, S. Hisaoka, H. Nishitani, and T. Matsuda, "Diffusion-weighted in vivo localized proton MR spectroscopy of human cerebral ischemia and tumor," *NMR in Biomedicine*, vol. 15, no. 1, pp. 69–74, 2002.

[20] D. Colvin, T. Yankeelov, M. Does, Z. Yue, C. Quarles, and J. Gore, "New insights into tumor microstructure using temporal diffusion spectroscopy," *Cancer Research*, vol. 68, no. 14, pp. 5941–5947, 2008.

[21] E. Wood, I. Ronen, A. Techawiboonwong, C. Jones, P. Barker, P. Calabresi, D. Harrison, and D. Reich, "Investigating axonal damage in multiple sclerosis by diffusion tensor spectroscopy," *The Journal of Neuroscience*, vol. 32, no. 19, pp. 6665–6669, 2012.

[22] Z. Liu, D. Zheng, X. Wang, J. Zhang, S. Xie, J. Xiao, and X. Jiang, "Apparent diffusion coefficients of metabolites in patients with MELAS using diffusion-weighted MR spectroscopy," *American Journal of Neuroradiology*, vol. 32, no. 5, pp. 898–902, 2011.

[23] F. Du, A. Cooper, T. Thida, A. Shinn, B. Cohen, and D. Öngür, "Myelin and axon abnormalities in schizophrenia measured with magnetic resonance imaging techniques," *Biological Psychiatry*, vol. 74, no. 6, pp. 451–457, 2013.

[24] Y. Bito, S. Hirata, T. Nabeshima, and E. Yamamoto, "Echo-planar diffusion spectroscopic imaging," *Magnetic Resonance in Medicine*, vol. 33, no. 1, pp. 69–73, 1995.

[25] S. Posse, E. Ackley, J. Zhang, and T. Zhang, "Diffusion tensor spectroscopic imaging in human brain," in *Proceedings of the 21st annual meeting of ISMRM*, p. 3956, International Society for Magnetic Resonance in Medicine, 2013.

[26] Y. Bito, Y. Kawai, K. Hirata, T. Ebisu, Y. Otake, S. Hirata, Y. Soutume, H. Ochi, M. Umeda, T. Higuchi, and C. Tanaka, "Diffusion tensor spectroscopic imaging of multiple metabolites in rat brains," in *Proceedings of the 21st annual meeting of ISMRM*, p. 3955, International Society for Magnetic Resonance in Medicine, 2013.

[27] A. Techawiboonwong, H. Kan, M. Versluis, W. A., and I. Ronen, "2D Diffusion weighted chemical shift imaging of brain metabolites at 7T," in *Proceedings of the 19th annual meeting of ISMRM*, p. 1444, International Society for Magnetic Resonance in Medicine, 2011.

[28] P. Bottomley, "Spatial localization in NMR spectroscopy in vivo," *Annals of the New York Academy of Sciences*, vol. 508, no. 1, pp. 333–348, 1987.

[29] T. Reese, O. Heid, R. Weisskoff, and V. Wedeen, "Reduction of eddy-current-induced distortion in diffusion MRI using a twice-refocused spin echo," *Magnetic Resonance in Medicine*, vol. 49, no. 1, pp. 177–182, 2003.

[30] I. Tkáć and R. Gruetter, "Methodology of 1H NMR spectroscopy of the human brain at very high magnetic fields," *Applied Magnetic Resonance*, vol. 29, no. 1, pp. 139–157, 2005.

[31] H. Gudbjartsson, S. Maier, R. Mulkern, I. Mórocz, S. Patz, and F. Jolesz, "Line scan diffusion imaging," *Magnetic Resonance in Medicine*, vol. 36, no. 4, pp. 509–519, 1996.

[32] L. Vanhamme, R. Fierro, S. Van Huffel, and R. de Beer, "Fast removal of residual water in proton spectra," *Journal of Magnetic Resonance*, vol. 132, no. 2, pp. 197–203, 1998.

[33] S. Smith, "Fast robust automated brain extraction," *Human Brain Mapping*, vol. 17, no. 3, pp. 143–155, 2002.

[34] Y. Zhang, M. Brady, and S. Smith, "Segmentation of brain MR images through a hidden Markov random field model and the expectation-maximization algorithm," *IEEE Transactions on Medical Imaging*, vol. 20, no. 1, pp. 45–57, 2001.

[35] S. Provencher, "Estimation of metabolite concentrations from localized in vivo proton NMR spectra," *Magnetic Resonance in Medicine*, vol. 30, no. 6, pp. 672–679, 1993.

[36] R. Nunes, P. Jezzard, and S. Clare, "Investigations on the efficiency of cardiac-gated methods for the acquisition of diffusion-weighted images," *Journal of Magnetic Resonance*, vol. 177, no. 1, pp. 102–110, 2005.

[37] L. Chang, D. Jones, and C. Pierpaoli, "RESTORE: robust estimation of tensors by outlier rejection," *Magnetic Resonance in Medicine*, vol. 53, no. 5, pp. 1088–1095, 2005.

[38] C. Pierpaoli, S. Marenco, G. Rohde, D. Jones, and A. Barnett, "Analyzing the contribution of cardiac pulsation to the variability of quantities derived from the diffusion tensor," in *Proceedings of the 11th annual meeting of ISMRM*, p. 70, International Society for Magnetic Resonance in Medicine, 2003.

[39] M. Garwood and L. DelaBarre, "The return of the frequency sweep: designing adiabatic pulses for contemporary NMR," *Journal of Magnetic Resonance*, vol. 153, no. 2, pp. 155–177, 2001.

[40] T. Scheenen, D. Klomp, J. Wijnen, and A. Heerschap, "Short echo time 1H-MRSI of the human brain at 3T with minimal chemical shift displacement errors using adiabatic refocusing pulses," *Magnetic Resonance in Medicine*, vol. 59, no. 1, pp. 1–6, 2008.

[41] J. Choi, A. Dedeoglu, and B. Jenkins, "Application of MRS to mouse models of neurodegenerative illness," *NMR in Biomedicine*, vol. 20, no. 3, pp. 216–237, 2007.

[42] R. De Graaf, *In vivo NMR spectroscopy: principles and techniques*. John Wiley & Sons, 2013.

[43] J. Snaar, W. Teeuwisse, M. Versluis, M. van Buchem, H. Kan, N. Smith, and A. Webb, "Improvements in high-field localized MRS of the medial temporal lobe in humans using new deformable high-dielectric materials," *NMR in Biomedicine*, vol. 24, no. 7, pp. 873–879, 2011.

[44] D. Bonekamp, M. Smith, H. Zhu, and P. Barker, "Quantitative SENSE-MRSI of the human brain," *Magnetic Resonance Imaging*, vol. 28, no. 3, pp. 305–313, 2010.